

JGR Planets

RESEARCH ARTICLE

10.1029/2020JE006492

Key Points:

- The effect of chemistry on the electrical properties of cores is important and should be accounted for as part of core cooling models
- Bulk chemistry significantly affects the power available to drive the dynamo during core cooling
- Thermal conductivities can change the dynamo cessation time significantly, by a billion years or more

Supporting Information:

Supporting Information S1

Correspondence to:

A. Pommier, pommier@ucsd.edu

Citation:

Pommier, A., Davies, C. J., & Zhang, R. (2020). A joint experimental-modeling investigation of the effect of light elements on dynamos in small planets and moons. *Journal of Geophysical Research: Planets*, 125, e20201E006492. https://doi.org/10.1029/2020JE006492

Received 22 APR 2020 Accepted 10 JUL 2020 Accepted article online 21 JUL 2020

A Joint Experimental-Modeling Investigation of the Effect of Light Elements on Dynamos in Small Planets and Moons

Anne Pommier¹, Christopher J. Davies², and Rong Zhang¹

¹Institute of Geophysics and Planetary Physics, Scripps Institution of Oceanography, University of California San Diego, La Jolla, CA, USA, ²School of Earth and Environment, University of Leeds, Leeds, UK

Abstract We present a joint experimental-modeling investigation of core cooling in small terrestrial bodies. Significant amounts of light elements (S, O, Mg, Si) may compose the metallic cores of terrestrial planets and moons. However, the effect of multiple light elements on transport properties, in particular, electrical resistivity and thermal conductivity, is not well constrained. Electrical experiments were conducted at 10 GPa and up to 1850 K on high-purity powder mixtures in the Fe-S-O(±Mg, ±Si) systems using the multianvil apparatus and the four-electrode technique. The sample compositions contained 5 wt.% S, up to 3 wt.% O, up to 2 wt.% Mg, and up to 1 wt.% Si. We observe that above the eutectic temperature, electrical resistivity is significantly sensitive to the nature and amount of light elements. For each composition, thermal conductivity-temperature equations were estimated using the experimental electrical results and a modified Wiedemann-Franz law. These equations were implemented in a thermochemical core cooling model to study the evolution of the dynamo. Modeling results suggest that bulk chemistry significantly affects the entropy available to power dynamo action during core cooling. In the case of Mars, the presence of oxygen would delay the dynamo cessation by up to 1 Gyr compared to an O-free, Fe-S core. Models with 3 wt% O can be reconciled with the inferred cessation time of the Martian dynamo if the core-mantle boundary heat flow falls from >2 TW to ~0.1 TW in the first 0.5 Gyr following core formation.

Plain Language Summary Different elements (like S, O, Mg, Si) are present in the metallic (Fe) cores of some planets and moons. The effect of these elements on the physical properties of the core is not well understood. Here we performed electrical experiments under pressure and temperature on different core compositions. The samples contain small amounts of S, O, Mg, and Si. Our experimental results show that at high temperature, the electrical response of the sample is significantly sensitive to the nature and amount of added elements. For each composition, we also estimated the ability of the sample to conduct heat. All these results were used as part of core cooling models. Our modeling results suggest that core chemistry significantly changes the energy available to power dynamo action during cooling. Applied to the core of Mars, our model shows a significant effect of oxygen on the activity of the core dynamo.

1. Introduction

The transport properties of iron alloys, such as electrical resistivity and thermal conductivity, strongly influence the evolutionary pathways of terrestrial planets and moons during cooling. In particular, these properties affect the generation of an intrinsic magnetic field by thermochemical convection in a fully or partially liquid core, as suggested by models of core evolution for the Earth (e.g., Davies, 2015; de Koker et al., 2012; Labrosse, 2015; Pozzo et al., 2012), Mars (e.g., Davies & Pommier, 2018; Williams & Nimmo, 2004), Mercury (e.g., Knibbe & van Westrenen, 2018), Ganymede (e.g., Rückriemen et al., 2015), and the Moon (e.g., Laneuville et al., 2014). Understanding how transport properties respond to changes in the thermal state, pressure, and core composition is fundamental to understanding core cooling processes and the generation of a magnetic field, as previous experimental work indicates that these properties are sensitive to temperature, pressure, and chemistry (e.g., Gomi et al., 2016; Ho et al., 1975; Pommier, 2018). The investigation of transport properties could also help estimate the content of light elements in planetary cores, which is not well constrained.

©2020. American Geophysical Union. All Rights Reserved.

POMMIER ET AL. 1 of 18



The nature and amount of light elements in the metallic core of a terrestrial body depends highly on the conditions during accretion and formation of the core. In particular, temperature, pressure, and redox conditions are among the main parameters that control the partitioning of light elements into the metallic core and their solubility (e.g., Buono & Walker, 2015; Dreibus & Wanke, 1985; Ohtani & Ringwood, 1984; Pozzo et al., 2019; Rubie et al., 2015; Tsuno et al., 2007). A few wt.% sulfur, oxygen, and silicon are thought to compose the cores of terrestrial planets and moons, because they partition to pure iron or iron-nickel alloys at pressure and temperature conditions, are abundant in the solar system, and are observed in meteorite geochemistry (e.g., Badro et al., 2015; Hirose et al., 2013; Poirier, 1994; Suehiro et al., 2017). Magnesium has also been suggested to be a potential candidate in the Earth's core, with the very high temperatures at the time of the core-mantle differentiation possibly allowing its partitioning into metal (Badro et al., 2016; O'Rourke & Stevenson, 2016). Cosmochemistry studies have suggested that carbon, hydrogen, and phosphorus are present in too small amounts (below 0.3 wt.%) to represent significant components of terrestrial cores (e.g., McDonough, 2003). In the Earth, several studies have pointed out that more than one element is likely present in the liquid outer core (e.g., Poirier, 1994; Alfé, 2002; Sanloup et al., 2004; Badro et al., 2007; Yokoo et al., 2019). Mercury's reducing conditions are consistent with a silicon-rich, sulfur-bearing core (e.g., Hauck et al., 2013; Namur et al., 2016; Cartier et al., 2020), while the more oxidizing conditions on Mars, the Moon, and possibly Ganymede are compatible with the presence of sulfur (e.g., Hauck et al., 2006; Kuskov & Belashchenko, 2016; Lodders & Fegley, 1997; Rückriemen et al., 2015) and oxygen in the core (Pommier et al., 2018; Tsuno et al., 2011).

Several studies have measured or computed the electrical resistivity and thermal conductivity of core analogues under pressure and temperature conditions. However, these investigations have focused mostly on systems that do not combine several light elements, considering either pure iron (e.g., de Koker et al., 2012; Pozzo et al., 2012 for computational studies, and Deng et al., 2013; Ohta et al., 2016; Konôpková et al., 2016; Silber et al., 2018 for laboratory studies) or binary systems such as Fe-S, Fe-Si, and Fe-O (e.g., de Koker et al., 2012; Pozzo et al., 2013; Wagle et al., 2019 for computational studies, and Gomi et al., 2013, 2016; Pommier, 2018; Silber et al., 2019 for laboratory studies). As pointed out by Wagle et al. (2019) using simulations at temperature ranging from 2000 to 8000 K and pressure from 23 up to >300 GPa, light elements do not affect electrical resistivity and thermal resistivity the same way: both S and Si atoms substitute for Fe in the molten state, but S atoms tend to distribute more evenly in liquid iron than Si atoms. In contrast, oxygen occupies interstitial sites, shortening Fe-O distances in the liquid state, which affects diffusive transport, and hence, increases electrical resistivity. It is unclear how light elements would affect transport properties when combined in metallic iron. The few investigations of the electrical and thermal properties of ternary systems are mostly computational and focused on the Fe-O-Si system at Earth's core pressure (Davies et al., 2015; Gubbins et al., 2015; Pozzo et al., 2013) and Fe-Si-S (Suehiro et al., 2017). The latter study performed electrical resistivity measurements at room temperature over the 40-110 GPa pressure range and used simulations to predict the electrical response of the Fe-Si-S alloy at high temperature. The electrical resistivity of an Fe-Si-S alloy was also measured experimentally at 6 GPa up to ~1950 K (Pommier et al., 2019). All these studies of ternary systems suggest high electrical resistivities as well as lower thermal conductivities than that obtained on pure iron. However, there is currently no investigation at pressure and temperature conditions relevant to planetary cores of the electrical and thermal properties of alloys containing a mixture of the four major light elements candidates expected in metallic cores, that is, S, O, Si, and Mg.

An important challenge for the electrical and thermal investigation of iron alloys regards the estimate of one physical property from the other. Electrical resistivity measurements are often used to estimate thermal conductivity at defined temperature using the Wiedemann-Franz law (Franz & Wiedemann, 1853), as thermal conductivity is particularly challenging to measure in the laboratory (e.g., Gomi & Hirose, 2015; Manthilake et al., 2019; Ohta et al., 2016; Pommier, 2018). It has been demonstrated for Fe-Ni at atmospheric pressure and above 1673 K and for Fe-Si alloys under a few GPa and up to 2100 K that the Wiedemann-Franz law underestimates the thermal conductivity of iron alloys, therefore providing a lower bound of thermal conductivity (Secco, 2017; Watanabe et al., 2019). The validity of the Wiedemann-Franz law has also been questioned for pure iron at high pressures and temperatures (Dobson, 2016; Konôpková et al., 2016; Ohta et al., 2016). This is due to the contribution of the thermal vibration of atoms to the thermal conductivity of iron alloys that is not accounted for in the Wiedemann-Franz law. It is likely that this equation also provides a lower bound for complex iron alloys containing several alloying agents, not only for alloys in binary

POMMIER ET AL. 2 of 18



Table 1 *Composition of the Starting Materials*

	Starting compositions									
Run #	System	O (wt.%)	S (wt.%)	Mg (wt.%)	Si (wt.%)	O (at.%)	S (at.%)	Mg (at.%)	Si (at.%)	
BB205	Fe-S-O	0.5	5.0	_	_	1.7	8.3	_	_	
BB206	Fe-S-O	3.0	5.0	_	_	9.4	7.8	_	_	
BB212	Fe-S-O-Mg	3.0	5.0	0.5	_	9.4	7.8	1.0	_	
BB213	Fe-S-O-Mg	3.0	5.0	2.0	_	9.2	7.7	4.0	_	
BB214	Fe-S-O-Mg	0.5	5.0	0.5	_	1.7	8.2	1.1	_	
BB219	Fe-S-O-Si	3.0	5.0	_	1.0	9.3	7.8	_	1.8	
BB245	Fe-S-O-Si ^a	3.0	5.0	_	1.0	9.3	7.8	_	1.8	
BB227	Fe-S-O-Si	3.0	5.0	_	0.1	9.4	7.8	_	0.2	
BB228	Fe-S-O-Si	0.5	5.0	_	0.1	1.7	8.3	_	0.2	
BB231	Fe-S-O-Si-Mg	0.5	5.0	0.5	0.1	1.7	8.2	1.1	0.2	

aSi added as FeSi2.

systems. One way to estimate the factor of correction on computed thermal conductivity estimates consists of comparing experimentally measured and computed thermal conductivities using the current thermal data set for iron alloys (e.g., Pommier, 2020; Secco, 2017).

Here we present a study of metallic cores containing multiple alloying agents using high-pressure experiments and core cooling modeling. In a first step, we performed electrical experiments on core analogues in the Fe-S-O(\pm Mg)(\pm Si) systems at 10 GPa and up to 1850 K. In a second step, experimental results were used to estimate thermal resistivity of the different alloys in the (partially) molten state, using a modified Wiedemann-Franz law. These estimates were then implemented into a 1-D parameterized model of core cooling. The effect of core chemistry on the generation and sustainability of the magnetic field in small terrestrial bodies is discussed. In particular, we apply our results to a Mars-type core and propose a detailed thermal history, following our previous study of the Martian core that considered an Fe-S chemistry (Davies & Pommier, 2018).

2. Joint Experimental-Modeling Approach

2.1. Experiments on Core Analogues

2.1.1. Starting Materials

Electrical experiments were performed on 10 analogues of planetary cores. Starting materials were powder mixtures of high purity (>99%) Fe, FeS, Fe $_2O_3$, MgO, SiO $_2$, and FeSi $_2$. The detailed compositions are listed in Table 1. The starting materials contained 5 wt.% S, up to 3 wt.% O, up to 2 wt.% Mg, and up to 1 wt.% Si. Compositions with the highest amounts of Mg and Si are considered end-member compositions of metallic cores. One starting material contained Si as FeSi $_2$ and all other Si-bearing samples contained Si as SiO $_2$ in order to test the effect of Si speciation on bulk resistivity. All the powders were stored in a vacuum oven at 383 K until use to minimize oxidation.

It should be noted that the starting materials are a mixture of different powders, as single-phase samples of iron alloys are challenging to synthesize (e.g., Mori et al., 2017). The starting materials not being single-phase alloys means that the materials below the melting temperature correspond to several phases coexisting (Fe, FeS, Fe₂O₃, \pm MgO, \pm SiO₂, and \pm FeSi₂), instead of a Fe–S-O(\pm Mg)(\pm Si) single phase. As previously shown for samples in the Fe-FeS system, the difference in bulk resistivity between multiphase materials and single-phase samples is not significant at pressure up to 8 GPa and temperature up to 2123 K (Pommier, 2018). We make the hypothesis that adding a small amount of O, Mg, or Si is unlikely to change the observations from Pommier (2018) about the effect of the number of phases on bulk resistivity at low temperature. However, investigating this topic is out of the scope of this paper and the application of the electrical results to planetary cores will only consider data collected at temperatures above 1900 K, that is, when the samples are partially or fully molten and correspond to metallic alloys.

POMMIER ET AL. 3 of 18

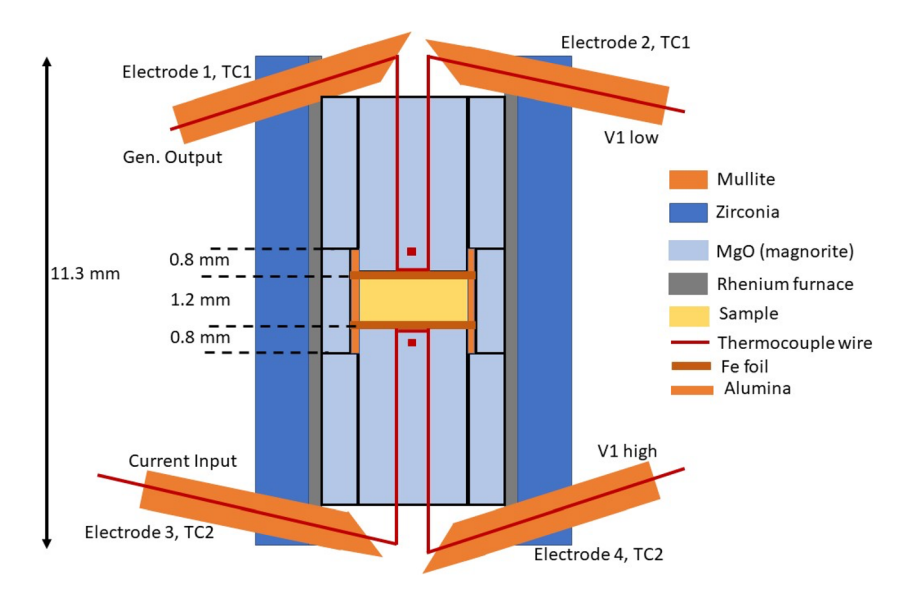


Figure 1. COMPRES electrical cell used for the four-electrode experiments in 14/8 multianvil assemblies. Thermocouple wires are also used as electrodes and are in contact with two Fe disks.

2.1.2. Electrical Experiments

Electrical experiments were conducted at 10 GPa and up to 1850 K in the multianvil apparatus at the Planetary and Experimental Petrology Laboratory at UCSD-SIO. Eight tungsten carbide cubes with a corner-truncation edge length of 8 mm and MgO octahedral pressure media with an edge length of 14 mm were used. A sketch of the COMPRES electrical cell assembly (Pommier et al., 2019) is presented in Figure 1. The cell is composed of three alumina rings that help keep the geometry of the sample during the experiment and contain the melt phase at high temperature. Two iron disks served as electrodes and a rhenium foil was used as a heater. Temperature was monitored using two Type-C ($W_{95}Re_5$ - $W_{74}Re_{26}$) thermocouples. All the MgO parts used in the cell assembly were fired at 1273 K for 2 hr or 1673 K for 1 hour. They were stored in a desiccator until use.

The experiments were conducted under quasi-hydrostatic conditions in the multianvil press using four-electrode electrical measurements. A dwell time was first applied to the sample at a temperature below the eutectic temperature (\sim 873 K) until a stable electrical response was obtained. In order to check the reproducibility of the electrical measurements, the electrical response of the sample was collected during both cooling and heating. Experiments were quenched at the highest temperature by shutting off the power to the heating system. The electrical resistance R was measured at each temperature using an impedance spectrometer (1260 Solartron Impedance/Gain-Phase Analyze) with a frequency range of about 40–1 Hz. The voltage was controlled by setting a DC potential of 1 V and an AC amplitude of either 500 or 1,000 mV.

The electrical resistivity ρ is calculated using the equation

$$\rho = R \times G$$
 (1)

where

$$G=2\pi r/l \tag{2}$$

with r being the radius of one electrode disk and l being the thickness of cylindrical sample. The uncertainty on the resistivity calculation, $\Delta \rho$, is listed for each experiment in Table 1. Because the iron electrode disks cover the surface of the sample and the middle alumina ring, they form a series circuit with the sample and sleeve, and their contribution to the measured bulk resistance was subtracted. The contribution of the alumina sleeve to the bulk resistance was neglected, since the resistance of alumina is several orders of magnitude higher than the resistance of the metallic sample (Pommier et al., 2019).

POMMIER ET AL. 4 of 18



2.1.3. Sample Analyses

After quenching, the recovered experimental samples were mounted in epoxy resin and carefully polished for analysis using scanning electron microscope (SEM) imaging at the UCSD-Nanoengineering Department. A FEI Quanta 600 SEM was used to characterize the texture of the samples. Energy dispersive X-ray spectrometry (EDS) with a voltage of 20 kV and an emission current of about 3.2 nA was used to analyze the phases of recovered samples as well as the starting composition of the powders.

2.2. Integration of Experimental Constraints Into a Core Cooling Model

2.2.1. Estimating the Thermal Conductivity of Core Analogues

The measured electrical resistivity data are used to calculate the thermal conductivity of the iron alloys as a function of temperature. Thermal conductivity corresponds to the sum of contributions of electrons and phonons scattering. In several metals, the electronic contribution to heat transport is significantly larger than the one due to transport by phonons (e.g., de Koker et al., 2012), therefore suggesting that the electronic component represents a lower bound, that is, at first approximation, an estimate of thermal conductivity. This lower bound (k_{LB}) can be calculated using the Wiedemann-Franz relationship:

$$k_{LB}=L\times T/\rho$$
 (3)

with L the Lorenz number with the theoretical value for the limit of electron degeneracy, called the Sommerfeld value, of $L_0 = 2.445 \times 10^{-8} \text{ W } \Omega \text{ K}^{-2}$ (Secco, 2017). The validity of the assumption that Equation 3 provides a reasonable estimate of the bulk thermal conductivity depends strongly on temperature, composition, and pressure (de Koker et al., 2012; Pozzo et al., 2012; Secco, 2017; Wagle et al., 2018). Using experimental values of electrical resistivity and thermal conductivity of iron, Secco (2017) showed that L/L_0 can vary by as much as 1.22 in the solid Fe and 1.32 in the molten state at pressures up to 6 GPa and temperatures up to 2100 K and that the deviation of L_0 at 1 atm is even higher than these values for Fe-Si alloys (but remains unclear under pressure). In Fe-O liquids, computations of k and ρ by de Koker et al. (2012) predicted a percentage deviation from L_0 of about 7-17% at the pressure conditions of our experiments (10 GPa) and at temperatures >2000 K. For Fe-Ni alloys, thermal conductivity measurements at 1 atm and under temperature indicate a difference between experimental thermal conductivities and estimates using Equation 3 of about 15-30% (using Holder, 1977; Kita & Morita, 1984; Seifter et al., 1998; Watanabe et al., 2019). Based on these observations from previous studies, we assume that the thermal conductivity k of our Fe-S-O alloys at 10 GPa can be estimated from electrical resistivity measurements ρ as a function of temperature assuming a 20% increase in the lower bound values computed using Equation 3. This represents an upper estimate rather than an upper bound, as we cannot rule out higher values of L. The effect of pressure on thermal conductivity can be estimated using the effect of pressure on electrical resistivity from previous studies of Fe-S and Fe-O alloys (Suehiro et al., 2017; Wagle et al., 2018, 2019). These works suggest that from 10 to 40 GPa, electrical resistivity decreases by ~10%. Therefore, we calculated the evolution of k as a function of both temperature and pressure over a pressure range of 10-40 GPa using the following equation:

$$k(T, P) = k(T) - (P - 10) \times 0.1/30 \times k(T)$$
 (4)

where

$$k(T) = 1.2 \times L_0 \times T/\rho \tag{5}$$

with T the temperature (K), P the pressure (GPa), 1.2 the temperature correction factor, and $(P - 10) \times 0.1/30$ the pressure correction factor.

2.2.2. Core Cooling Modeling

We calculated the thermal and chemical evolution of a Mars-sized core over the last 4.5 Gyr using a 1-D parameterized model. Full details of the model can be found in Davies and Pommier (2018), and so only a brief description is given here. The core is initially entirely liquid with a prescribed starting temperature and bulk composition. The liquid region of the core is always assumed to be vigorously convecting such that the composition is uniform and the temperature profile follows an adiabat. In the absence of core crystallization, the core-mantle boundary (CMB) heat flow Q_{cmb} is balanced by the heat Q_s stored in the core.

POMMIER ET AL. 5 of 18

Although the model allows for core crystallization at arbitrary depth, we focus on top-down crystallization as this core cooling regime has been suggested previously for Mars, Ganymede, and the Moon (Breuer et al., 2015; Davies & Pommier, 2018; Rückriemen et al., 2015; Stewart et al., 2007). In this regime, freezing of the metallic core begins from the CMB because the melting curve T_m is shallower than the adiabatic gradient (e.g., Breuer et al., 2015; Stewart et al., 2007). The solid phase is assumed to be heavier than the residual liquid and therefore "snows" into the deeper core where it remelts. Generation of snow releases latent heat Q_L^s and gravitational energy Q_g^s as solid particles sink through the snow zone. Remelting of snow absorbs an amount of latent heat Q_L^l and releases further gravitational energy Q_g^l since the remelted liquid is enriched in iron (and therefore denser) compared to the bulk core. An amount of latent heat Q_L^B is released at the base of the growing snow zone, though this contribution is small enough to neglect (Davies & Pommier, 2018). These processes affect the power E_J ("dynamo entropy") that is available to generate the intrinsic magnetic field.

The cooling model solves the global energy, entropy and mass balance equations that describe the long-term evolution of the core (e.g., Breuer & Moore, 2015; Nimmo, 2015). The core comprises a snow layer on the liquidus above a vigorously convecting core. The model relies on the following four main assumptions: (1) All light elements remain in the liquid phase on freezing; (2) melting is fast, that is, instantaneous relaxation to phase equilibrium; (3) sinking and remelting of solid iron is rapid; and (4) an adiabatic temperature profile exists throughout the core. With these approximations the global energy and entropy balances are (Davies & Pommier, 2018)

$$Q_{cmb} = Q_s + Q_g^s + Q_L^l + Q_L^s + Q_L^l + Q_L^B = Q \frac{dT_c}{dt}$$
 (6)

$$E_{J} + E_{k} = E_{s} + \frac{Q_{g}^{s} + Q_{g}^{l}}{T_{c}} + E_{L}^{s} + E_{L}^{l} + Q_{L}^{B} \left(\frac{T_{c} - T(r_{s})}{T_{c}T(r_{s})} \right) = {^{\sim}} E \frac{dT_{c}}{dt}.$$
(7)

Here E_k is the entropy due to thermal conduction, which depends on the thermal conductivity, and the terms E_L^s and E_L^l are entropy terms that reflect the thermodynamic efficiency of the heat sources Q_L^s amd Q_L^l in Equation 6. T_c is the CMB temperature and r_s is the radius of the base of the snow zone (if one exists). Note that k does not appear in the energy balance (Equation 6) and hence models that differ only in the choice of k produce the same thermal history; however, these models produce different magnetic histories through Equation 7.

Equation 6 relates Q_{cmb} to the core cooling rate, $\mathrm{d}T_c/\mathrm{d}t$, which can be used to compute the dynamo entropy E_J , which must be positive for dynamo action. The time when E_J first passes from positive to negative values defines the termination point of the dynamo. In the case of Mars, the key observation pertaining to core dynamics is that the global magnetic field (and hence dynamo) likely decayed around 4.1–3.8 Ga (Acuña et al., 1998; Langlais et al., 2012; Weiss et al., 2002). The variables ${}^\sim Q$ and ${}^\sim E$ are integrals that depend on the properties of the core material. The model also outputs the properties of a snow zone at the top of the core if one exists. The base of the snow zone is defined as the radius where the adiabat intersects the melting curve; if the core does not cool to the melting point at the CMB then no snow zone forms. All the default parameters used are from Davies and Pommier (2018) with the exception of k and Q_{cmb} , which are described below.

Here, unlike previous work, we explicitly model the temperature-dependence of k on the thermal evolution of the core. We use the new k values derived from electrical experiments under temperature. To do so, thermal conductivity estimates are expressed as a polynomial equation which is evaluated at the current temperature at each depth (Table S1 in the supporting information). This gives the radial variation of thermal conductivity as k(P(r), T(r)).

The CMB heat flow is an input to the model that must be specified over the 4.5 Gyr evolution. In principle Q_{cmb} can be calculated using a parameterized model of mantle convection that is coupled to the core evolution (e.g., Williams & Nimmo, 2004), thus allowing changes in core temperature to alter the heat flow. Here we choose a simpler approach that introduces fewer uncertain parameters than that used in a core-mantle parameterized model and allows us to focus on the role of core thermal conductivity in the core thermal-magnetic history. We write Q_{cmb} using a simple functional form,

POMMIER ET AL. 6 of 18

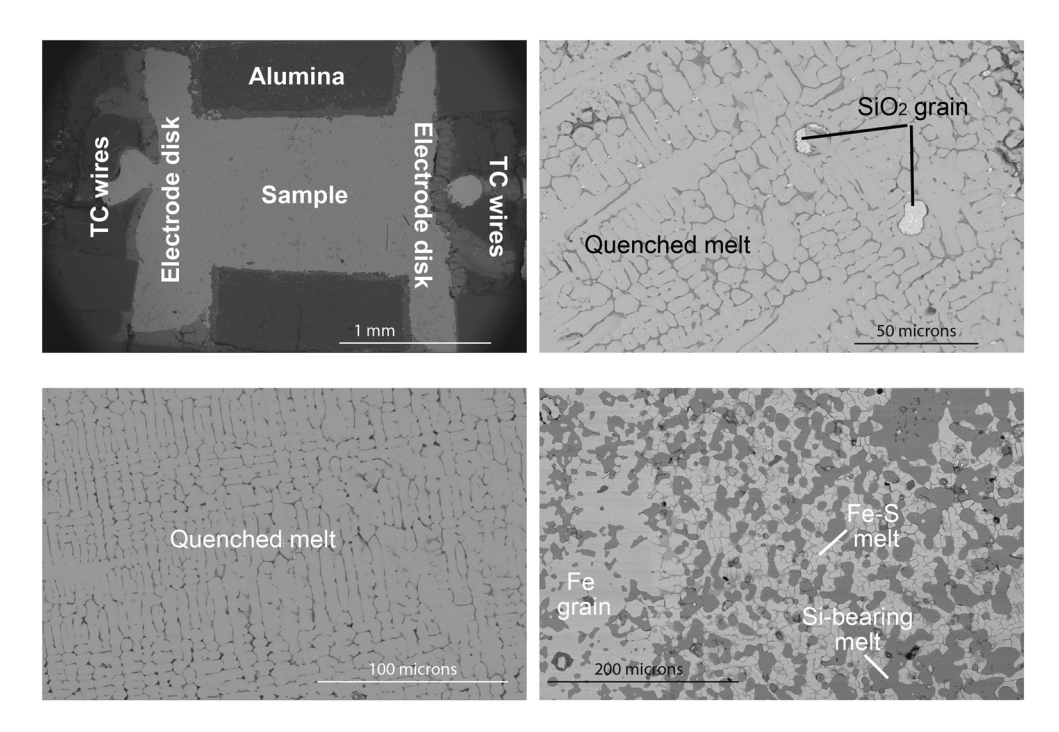


Figure 2. SEM images of selected recovered samples. (top left) Fe-S-O-Si sample quenched at 10 GPa and 1772 K. The two electrode disks and thermocouple wires are visible. A small layer (Al-bearing alloy) is formed at the sample-alumina interface and has a negligible effect on the electrical measurement (Pommier & Leinenweber, 2018). (top right) Fe-S melt and SiO_2 grains in $FeS_5O_3Si_1$ sample. (bottom left) Quenched melt texture in an Fe-S-O sample. (bottom right) Quenched melt in the Fe-S-O-Si sample.

$$Q_{cmb} = Q_p + Q_f e^{-t/\tau} \tag{8}$$

where t is time, $Q_p + Q_f$ is the heat flow at t = 0 and τ is a time scale. By varying Q_p , Q_f , and τ it is possible to closely reproduce previously published time series of Q_{cmb} for Mars (Leone et al., 2014; Thiriet et al., 2019; Williams & Nimmo, 2004). In particular, values of $Q_p = 0.2$ TW, $Q_f = 1.3$ TW, and $\tau = 0.9$ Gyr closely represent the time series of Q_{cmb} from Williams and Nimmo (2004) that was used in Davies and Pommier (2018). The prescription (8) also makes it easy to develop new time series that have certain desirable properties. We will show that the range of experimental k values produce a broad range of dynamo termination times that cannot be reconciled with the observations by simply changing core properties within reasonable bounds. By using Equation 8 it is possible to reproduce the observed termination time for all of the different k values.

3. Results

3.1. Experimental Results

Textural and chemical analyses of retrieved samples after electrical experiments using the EDS-SEM techniques are presented in Figure 2 and Figure S1 in the supporting information. The interface between the sample and the alumina ring is characterized by a thin (< ~30 micron thick) layer of Al-bearing alloy, which does not affect the sample's bulk electrical response (Pommier & Leinenweber, 2018). Some samples present a small amount of W in the dendritic phase, which is consistent with unavoidable interactions with the thermocouple wires at high temperature. No strong compositional heterogeneity is observed across the recovered samples. SEM images of recovered samples are shown in Figure 2. The retrieved Fe-S-O and Fe-S-O-Si (with Si added as FeSi₂) samples present textures of fully molten alloys following rapid solidification. Mg-bearing alloys and alloys containing Si as SiO₂ were only partially molten (Figure 2), in agreement with the fact that the melting point of MgO (~3800 K; Kimura et al., 2017) and SiO₂ (~3100 K; Zhang et al., 1993) at 10 GPa is higher than the melting point of the Fe electrode disks (~2100 K; Buono & Walker, 2011), which constrains the quenching temperature of the experiments. The electrical cell geometry was well-preserved

POMMIER ET AL. 7 of 18

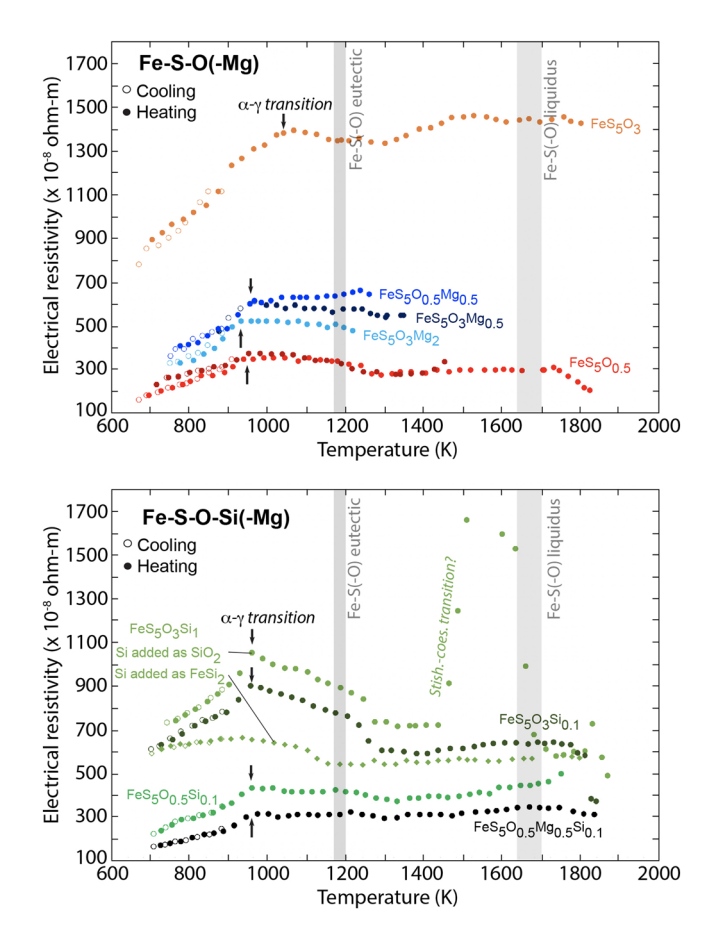


Figure 3. Electrical resistivity results as a function of temperature for the different alloy compositions. The α - γ transition is indicated with black arrows. Eutectic temperature for Fe-S at 10 GPa is from Chen et al. (2008), and references therein. (top) Results for the two Fe-S-O alloys and three Mg-bearing alloys. (bottom) Results for the five Si-bearing alloys.

during the experiment (Figure 2), minimizing uncertainty on the geometric factor calculations and hence, on electrical resistivity. Dendritic patterns are visible in all samples, and color contrasts are observed between dendritic structures and the surrounding phase, indicating different chemistry (Supplementary Figure S1). In particular, the presence of S in the quenched phase surrounding the dendrites increases the color contrast between the two phases.

Electrical resistivity results are presented as a function of temperature in Figure 3. In all experiments, electrical data collected after the dwell time during cooling and second heating demonstrate data reproducibility. Reproducibility was also checked by the repeat of the experiment on the FeS₅O_{0.5} material. For all samples except the one containing Si as FeSi2, electrical resistivity increases significantly with increasing temperature until the α - γ transition. This phase transformation of iron is clearly identified and it is located around 1000 K (±50 K). From 1000 to 1300 K, the Si-bearing alloys present a small decrease in resistivity, whereas the resistivity of the other alloys is not temperature-dependent, at first approximation. The onset of melting is not as clearly identified as the α - γ transition but corresponds for most samples to a slight inflection in resistivity at 1200-1300 K. This temperature is in good agreement with the eutectic temperature for Fe-S at 10 GPa (e.g., Chen et al., 2008). Above 1200-1300 K, all alloys except the one containing Si as SiO₂ display a temperature-independent electrical response.

Figure 3 also illustrates the effect of starting composition on electrical resistivity. The two samples of bulk composition ${\rm FeS_5O_3Si_1}$ present contrasting resistivities below 1700 K and a similar electrical response at T>1700 K; the difference in electrical behavior can be attributed to Si, which is either added as ${\rm SiO_2}$ (silicate) or ${\rm FeSi_2}$ (metal). At T>1700 K, the melt phase dominates the samples' resistivity; their similar electrical response confirms that both samples have a similar bulk composition and suggests that, in the ${\rm SiO_2}$ -bear-

ing sample, some Si partitioned into the metallic liquid. The SiO_2 -bearing starting powder is more resistive below 1700 K and the α - γ transition is more visible than in the $FeSi_2$ -bearing powder. An abrupt change in resistivity is observed in the SiO_2 -bearing sample at ~1500–1673 K (Figure 3). Such a peak in electrical resistivity is not observed in the $FeSi_2$ -bearing sample nor in any other SiO_2 -bearing samples that all contain less Si than 1 wt.% (Table 1).

The effect of alloy chemistry on bulk electrical resistivity is presented in Figures 3 and 4. Electrical results indicate that, at the conditions of the experiments, adding Mg tends to decrease the resistivity of iron alloys. For instance, at 1100 K, the Fe-S-O alloy containing 2 wt% Mg has a resistivity that is 12.5% lower than the alloy containing 0.5 wt.% Mg (Figure 3). In contrast, adding O and/or Si increases the bulk electrical resistivity. Over the investigated temperature range, FeS_5O_3 is about 4.8 times more resistive than $FeS_5O_{0.5}$ (Figure 3, top plot; Figure 4). This factor decreases to 1.4–2.1 when 0.1 wt.% Si is added (Figure 3, bottom plot; Figure 4). Fe-S-O-Si samples containing the same amount of S and O present an increase in resistivity with increasing Si content when Si is added as SiO_2 . The sample containing both Mg and Si is the least resistive Si-bearing alloy. As illustrated in Figure 4, at defined temperature, Fe-S-O and Fe-S-O-Si samples show a stronger dependence of resistivity to the total amount of alloying agent than Fe-S-O-Mg samples.

3.2. Thermal Conductivity of Core Analogues

Thermal conductivity estimates are presented for the different compositions at T > 1200 K and at 10 GPa in Figure 5. These estimates were obtained using the linear extrapolation of electrical resistivity measured at $T \ge 1100$ K to the temperature range of 1900–3100 K; the extrapolated values of ρ were then implemented

POMMIER ET AL. 8 of 18

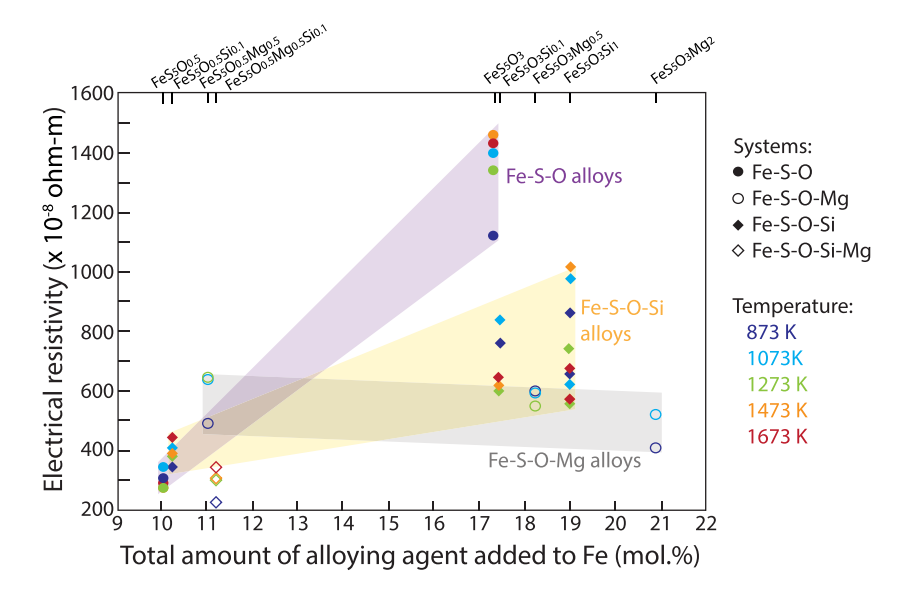


Figure 4. Electrical resistivity as a function of the total amount of alloying agents. Colors correspond to different temperatures. The shaded areas only represent a guide for the eye.

into Equations 4 and 5 to calculate k (T,P). The linear fits to compute k using Equation 5 are listed in Table S1 in the supporting information. The FeS₅O₃ sample is characterized by the lowest thermal conductivity, whereas FeS₅O_{0.5} and the sample containing both Mg and Si show the highest values. All other alloys display intermediate thermal conductivity values. For all samples, heat transport increases with increasing temperature. Thermal conductivity has been extrapolated to temperatures up to 3100 K for three selected samples: FeS₅O₃, FeS₅O_{0.5}, and FeS₅O₃Mg_{0.5}, representing, respectively, a lower bound, an upper bound, and an intermediate case of thermal conductivity of core analogues. Over the 1000–3100 K

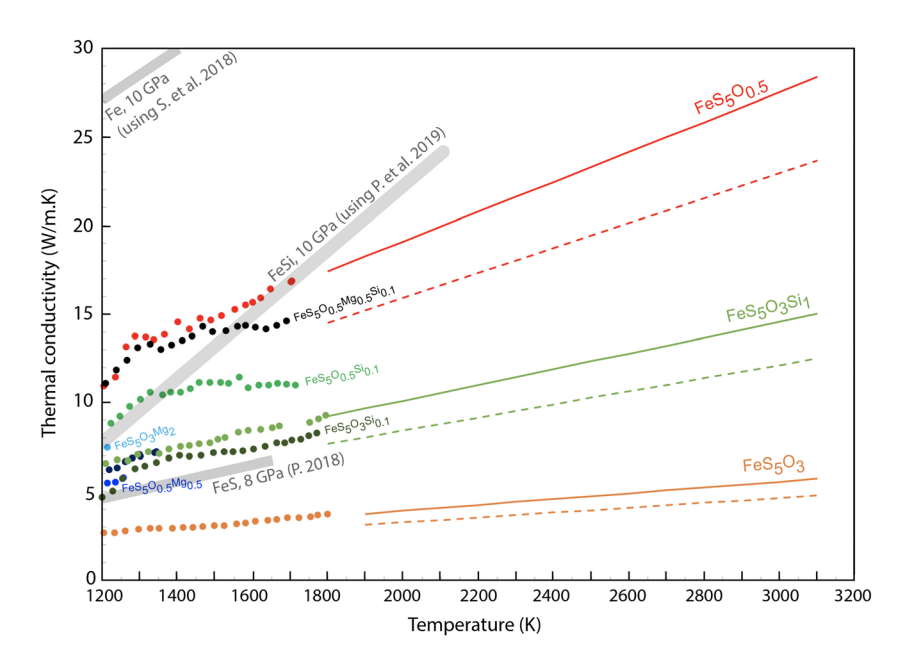


Figure 5. Thermal conductivity of iron alloys at 10 GPa as a function of temperature and extrapolation for selected samples up to 3100 K. the color code is similar to the one used in Figure 3. Solid lines correspond to extrapolation using Equation 4, dashed lines correspond to extrapolations using the Wiedemann-Franz law. As a comparison, thermal conductivity estimates were calculated for FeSi using electrical resistivity data at 10 GPa from Pommier et al. (2019), for FeS using electrical resistivity data at 8 GPa (Pommier, 2018), and for Fe using electrical resistivity data at 9 and 11 GPa from Silber et al. (2018).

POMMIER ET AL. 9 of 18

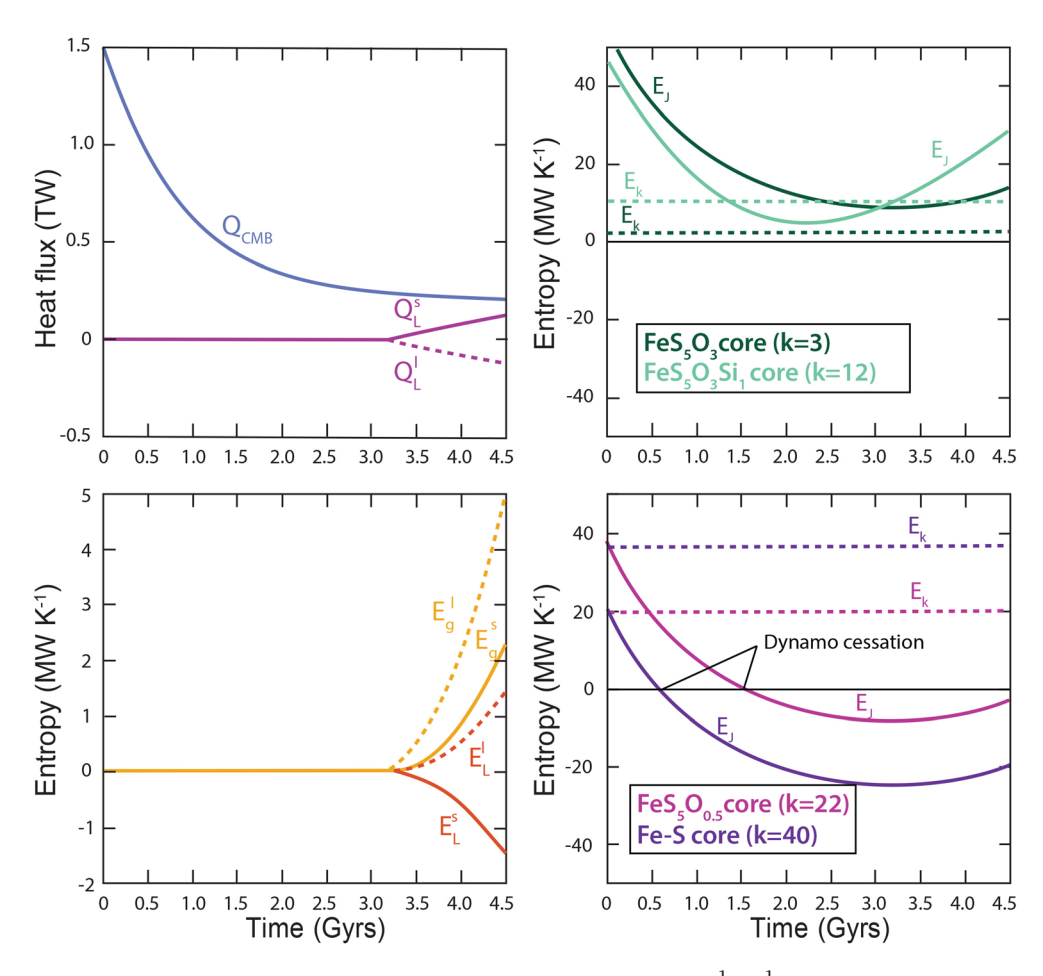


Figure 6. Modeling results for constant k values ranging from 3 to 40 W m⁻¹ K⁻¹corresponding to different core chemistry. Top left: heat flux as a function of time; bottom left: entropy terms that reflect the thermodynamic efficiency of the heat sources as a function of time; top right and bottom right: time evolution of the dynamo entropy and entropy due to thermal conduction for four different k values. The dynamo stops for all cases except k = 3 W m⁻¹ K⁻¹. Our model reproduces the data of Davies and Pommier (2018) for k = 40 W m⁻¹ K⁻¹. See text for details.

range, thermal conductivity increases by a factor of 3.4, 4.0, and 2.6 for $FeS_5O_{0.5}$, $FeS_5O_3Mg_{0.5}$, and FeS_5O_3 , respectively. We notice that thermal resistivity variations among samples increase only slightly with increasing temperature: for example, at 1000 K, $FeS_5O_{0.5}$ is 3.8 times more thermally conductive than FeS_5O_3 and at 3100 K, this factor increases to 5 (Figure 5). For comparison, extrapolations using the Wiedemann-Franz law (Equation 3) are plotted (dashed lines); as predicted by Equation 5, a difference in thermal conductivity of up to 20% is observed between estimates using this equation (which represents a lower bound) and the modified relationship.

3.3. Modeling Results

The core cooling model described in section 2 was applied to a Mars-sized metallic core, considering the three selected core compositions (FeS₅O_{0.5}, FeS₅O₃Si₁, and FeS₅O₃) and k values obtained at 10 GPa, extrapolated up to 40 GPa and to 3100 K. Mg-bearing core compositions are not considered here as it is unlikely that much Mg is dissolved in the metal (e.g., Badro et al., 2016). Figure 6 presents the contributions of individual terms to the energy and entropy balances for four models with constant values of k = 3,12,22, and 40 W m⁻¹ K⁻¹, which approximately correspond to the mean k values for the compositions FeS₅O_{0.5}, FeS₅O₃Si₁, FeS₅O₃, and the Fe-S core considered in Davies and Pommier (2018) across the relevant temperature range. In this figure, the CMB heat flow of Williams and Nimmo (2004) was represented using Equation 8 with $Q_p = 0.2$ TW, $Q_f = 1.3$ TW, and $\tau = 0.9$ Gyr, which closely reproduces the original time series. As previously observed in our Fe-S core cooling study, the latent heat terms Q_1^s and Q_1^1 almost

POMMIER ET AL. 10 of 18

counterbalance each other since the same amount of mass is produced and destroyed; the difference is due to the fact that heat is released throughout the snow zone but absorbed only at the top of the liquid region. The corresponding entropy terms make a significant contribution to the entropy balance only in the most recent times as can be seen from the upturn in the E_J time series. The only difference between the four cases is in the time series of E_k and E_J : the lower the thermal conductivity, the lower the value of E_k and the longer the dynamo operates (Figure 6, right panels). The key result is that, all other factors being equal, lowering k substantially increases the lifetime of the dynamo: for k = 40 W m⁻¹ K⁻¹, the dynamo fails after ~0.5 Gyr; whereas the dynamo does not stop when k = 12 and 3 W m⁻¹ K⁻¹. In terms of core chemistry, low k values are obtained for O-rich alloy compositions (Figure 5).

The difference in dynamo termination times observed in Figure 6 cannot simply be reconciled by uncertainties in core material properties. We considered an "extreme" parameter combination based on the values in Davies and Pommier (2018), Table 1) that would lead to the earliest dynamo termination time (see Figure 6 of Davies & Pommier, 2018). This parameter set consists of $k = 22 \text{ W m}^{-1} \text{ K}^{-1}$, a CMB pressure to 23 GPa (default value 21 GPa), a CMB radius to 1,800 km (default 1,627 km), and initial core temperature to 2500 K (default 2400 K). However, we found the extreme parameter combination reduced the dynamo lifetime by only ~0.4 Gyr compared to that shown in Figure 6, which is not nearly enough to account for the variability induced by the differences in conductivity values. Since snow zones do not form until long after the dynamo has failed (e.g., Figure 6) this result is independent of melting and partitioning behavior. Therefore, in order to determine whether it is possible to find thermal-magnetic histories with each value of k that are consistent with the observed dynamo termination time we considered modifications to the CMB heat flow.

To investigate this point we used the default parameters from Davies and Pommier (2018) and constant k except that the CMB heat flow is modified using Equation 8 in order to obtain an E_J that falls below zero around 4 Ga. The results are presented in Figure 7, in which Q_c was changed using Equation 8 in order to ensure a dynamo cessation time of ~0.5 Gyr, in agreement with Mars's magnetic history. Figure 7 shows that varying Q_{cmb} allows all three models to reproduce successfully the dynamo cessation time, implying that core thermal histories based on O-bearing alloys are consistent with this fundamental constraint on Martian core evolution. The parameterized Q_{cmb} time series are also broadly consistent with published values obtained from coupled core-mantle evolution models. For the FeS₅O_{0.5} composition, the Q_{cmb} time series lies between those obtained by Williams and Nimmo (2004) and Leone et al. (2014). For the FeS₅O_{0.3}Si₁ composition, the initial drop in Q_{cmb} is similar to the results of Thiriet et al. (2019), while the long-term steady heat flow is reasonably consistent with this study and that of Leone et al. (2014).

Figure 7 also illustrates the effect of k(T) on core cooling. The temperature-dependence of k is unimportant compared to the mean value (taken to be either 3, 12, or 22 W m⁻¹ K⁻¹, depending on the core composition). For all three cases, considering a constant k value or a temperature-dependent thermal conductivity (k(T)) leads to a similar cessation time for the dynamo. This result is consistent with the small temperature dependence of k (Figure 5): in the FeS₅O_{0.5} case, a 1000 K drop in temperature leads to only a ~5 W m⁻¹ K⁻¹ drop in thermal conductivity.

Finally, we note that none of the models for the three cases in Figure 7 produce a snow zone as the core temperature remains above the liquidus temperature of Fe-S-O system for all time (Buono & Walker, 2015; Huang et al., 2010; Pommier et al., 2018; Terasaki et al., 2011; Urakawa et al., 1987).

4. Discussion

4.1. Electrical and Thermal Properties of S,O-Bearing Iron Alloys at High Temperature

The electrical resistivity of all investigated alloys at 10 GPa and 1200–1850 K varies from $\sim 3 \times 10^{-6}$ to 15×10^{-6} ohm-m (or 300 to 1,500 microhm-cm) (Figure 3) and is highly sensitive to bulk composition (Figures 3 and 4). The strong dependence of resistivity to chemistry is in agreement with previous studies of Fe, Fe-S, Fe-Si, and Fe-P alloys under a pressure of a few GPa and confirms that adding light elements to pure iron increases resistivity (Deng et al., 2013; Manthilake et al., 2019; Pommier, 2018; Pommier et al., 2019; Silber et al., 2019; Yin et al., 2019). The alloys in our study all contain 5 wt.% S (Table 1) and their resistivities are higher than the ones measured for FeS₅ at 8 GPa and up to 1573 K ($<1 \times 10^{-6}$ ohm-m, or 100

POMMIER ET AL. 11 of 18

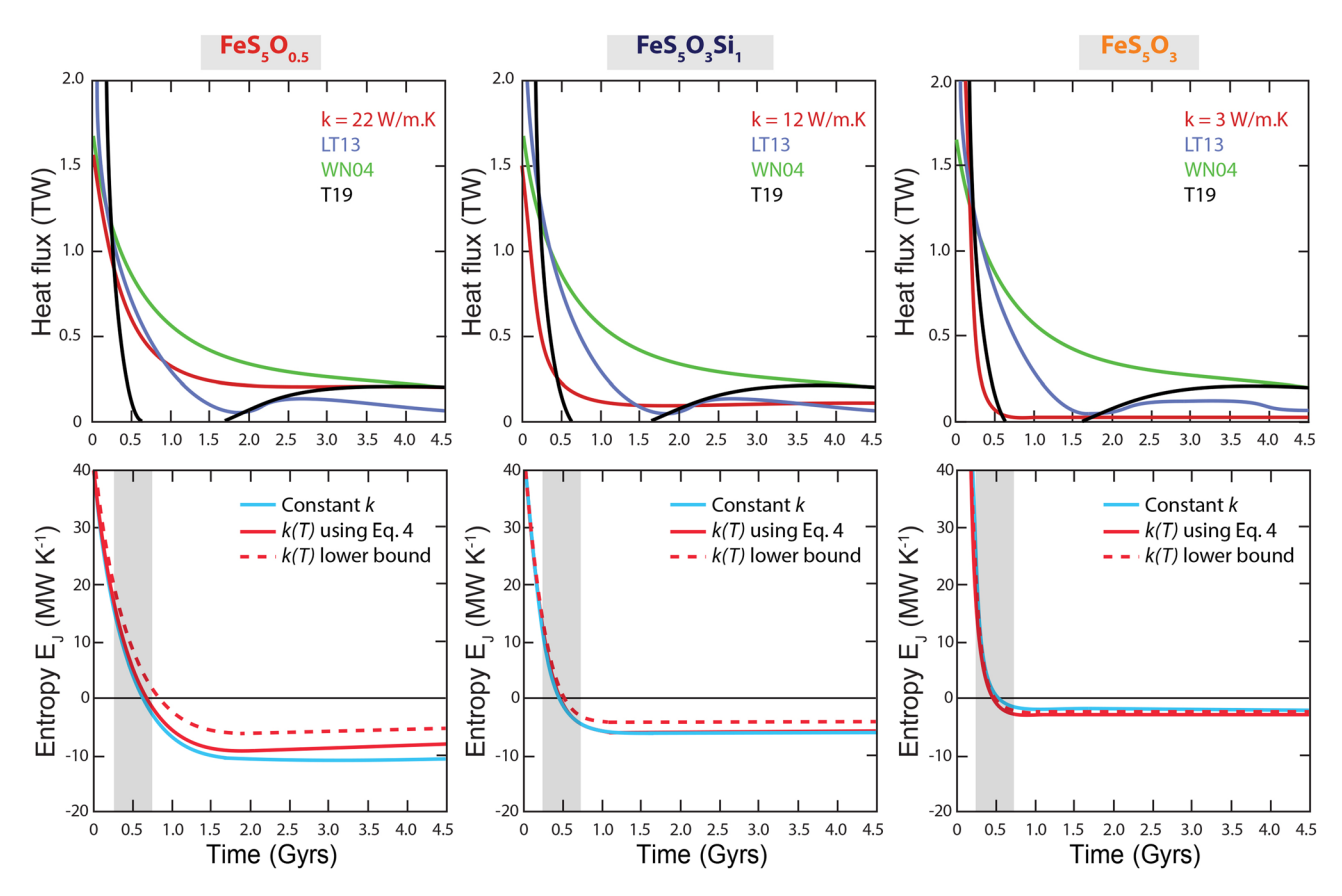


Figure 7. Modeling results for a FeS₅O_{0.5} core (left panels), a FeS₅O₃Si₁ core (middle panels), and a FeS₅O₃ core (right panels). Top plots show the core-mantle boundary heat flow Qc from the published models of Williams and Nimmo (2004) (WN04), Leone et al. (2014) (LT13), and Thiriet et al. (2019) (T19) together with the parameterized curve (red) that gives a dynamo cessation time around 4 Ga with a constant value of k (either 22, 12, or 3 W m⁻¹ K⁻¹). The bottom panels show the dynamo entropy E_J over time for the case of a constant k value (blue) and two temperature-dependent k values (red). The dynamo cessation occurs when E_J becomes negative. The gray areas in the bottom panels correspond to the dynamo cessation time predicted for an Fe-FeS Martian core by Davies and Pommier (2018) (see text for details).

microhm-cm, Pommier, 2018). The pressure difference is unlikely to explain the contrast in the electrical response, because increasing pressure decreases Fe-S resistivity (Pommier, 2018; Suehiro et al., 2017). This comparison between FeS₅ and Fe-S-O alloys suggests that even a small amount of oxygen (0.5 wt.%) has a strong effect on electrical and thermal properties. Moreover, the properties of Fe-S-O alloys are in the same range of magnitude as the ones for FeS at 8 GPa (Pommier, 2018; Figure 5). The relative effects of S and O can be explained from their respective structural behavior in the iron alloy. Structural studies of Fe-S alloys pointed out that increasing the S content decreases the effective electron mean free path in Fe-S liquids, which increases scattering due to impurity and hence, increases electrical resistivity (Wagle et al., 2018). In contrast, oxygen is less capable than sulfur to decrease the mean free path, because its bonding with iron is less efficient and contrary to sulfur, its atomic size is not similar to the one of an iron atom (Alfè & Gillan, 1998; Wagle et al., 2018). Our results also show a strong difference in transport properties between FeS₅O_{0.5} and FeS₅O₃ (Figures 3-5). This is in agreement with first-principle simulations that predicted a significant effect of the O content on the electrical and thermal properties of Fe-O liquids and observed that increasing the amount of oxygen increases electrical resistivity and decreases thermal conductivity (de Koker et al., 2012; Wagle et al., 2019). As highlighted by Wagle et al. (2019), oxygen atoms occupy interstitial sites in the iron alloy. This shortens the Fe-O distances, which results in a less efficient diffusive transport of charge than in an O-free iron alloy.

At T > 1200 K, the Si-bearing and Mg-bearing Fe-S-O alloys present electrical resistivities and thermal conductivities that range between the values obtained for FeSO_{0.5} and FeSO₃ (Figures 3 and 5). As illustrated in Figure 4, adding Si to an Fe-S-O alloy tends to decrease its electrical resistivity, although a clear trend is not observed. Thermal conductivities of Si-bearing alloys present a lower temperature dependence than the

POMMIER ET AL. 12 of 18

Table 2
Experimental Conditions For Electrical Resistivity Measurements

Run #	System	P (GPa)	T range (K)	Dwell time (hr)	Uncertainty on resistivity (%) ^a
BB205	Fe-S-O	10	668-1823	2	8.2-12.0
BB226	Fe-S-O	10	714-1451	1.5	4.2-8.2
BB206	Fe-S-O	10	669-1799	2	5.0-6.2
BB212	Fe-S-O-Mg	10	873-1345	2	3.9-7.6
BB213	Fe-S-O-Mg	10	748-1216	1.5	6.1–7.5
BB214	Fe-S-O-Mg	10	750-1258	1.5	6.3-8.1
BB219	Fe-S-O-Si	10	739-1867	1.2	5.2-7.8
BB227	Fe-S-O-Si	10	699-1838	2.2	5.1-7.2
BB228	Fe-S-O-Si	10	706-1747	1.5	4.3-9.5
BB245	Fe-S-O-Si	10	701-1794	1.8	4.7-5.1
BB231	Fe-S-O-Si-Mg	10	705–1833	1.5	7.0–10.9

 $^{^{}a}\Delta\rho = |\pi r^{2}/l| \times \Delta R + |2\pi Rr/l| \times \Delta r + |-\pi Rr^{2}/l^{2}| \times \Delta l$ with ρ the resistivity, l the sample thickness, R the electrical resistance of the sample, and r the radius of the electrode disk covering the sample.

conductivities calculated from electrical measurements on FeSi at the same pressure (Pommier et al., 2019). These observations might reflect a competing effect between Si and O atoms, though structural studies of FeS-O-Si liquids are needed to fully explain the experimental data. Experimental and modeling structural data on Fe-Si alloys proposed that Si is integrated in liquid iron via substitution mechanisms and that Fe-Si alloys approach the close-packing limit of twelvefold coordination (e.g., Morard et al., 2008; Wagle et al., 2019). For similar concentrations and the considered pressure range (10–40 GPa), silicon and sulfur are supposed to have a stronger effect on electrical resistivity than oxygen (Wagle et al., 2019), which leads to the hypothesis that the electrical data on Si-bearing alloys are controlled primarily by S and Si, not O. However, our experiments do not allow exploring the behavior of Si and or Mg in the liquid as samples had to be quenched before reaching the melting temperature of SiO_2 and of MgO (to avoid melting of the electrodes).

The peak in electrical resistivity observed at ~1500–1673 K in the $FeS_5O_3Si_1$ sample with Si added as SiO_2 (Figure 3) is consistent with the temperature of the stishovite-coesite transition at this pressure (Zhang et al., 1993). Understanding the magnitude of this electrical peak requires further experiments and this is out of scope of the present study. At 10 GPa, phase equilibria studies showed that the liquidus of SiO_2 is higher than the quenching temperature of the experiment (e.g., Zhang et al., 1993; Table 2). Therefore, this alloy consists of an Fe,S,O-rich liquid that contains small amounts of Si and a few isolated SiO_2 grains, as illustrated by SEM-EDS data (Figure 2). Increasing temperature increases the ability of the liquid to dissolve oxygen (e.g., Pommier et al., 2018), which is consistent with the absence of solid Fe_2O_3 or FeO grains in the quenched samples.

The intermediate case in our core models has an FeS₅O₃Si₁ composition. At temperature above the eutectic composition, this material is composed of two phases: a highly conductive metallic liquid and resistive SiO₂ grains. Several models have been developed to predict the bulk conductivity of multiphase materials as a function of a conductive interstitial phase (e.g., Glover et al., 2000; ten Grotenhuis et al., 2005, and references therein). Connectivity can be probed using the percolation theory (Stauffer & Aharony, 1992), in which the connectivity threshold depends on the geometry of the conductive network (e.g., Miller et al., 2015). In many ways, the geometry we address here is analogous to the melt-grain networks analyzed by Miller et al. (2015), except that the liquid phase in our materials is a metallic melt, not a silicate one. To understand the effect of SiO₂ grains on the bulk electrical response of this core, we calculated the bulk electrical resistivity as a function of melt fraction (Figure S2 in the supporting information). The metallic liquid was considered to be either FeS₅O₃ or FeS₅O_{0.5} and its resistivity comes from our experiments. The electrical resistivity of SiO₂ at 20 GPa and 1800 K is from Scipioni et al., 2017 (it was extrapolated to 1800 K). We used the geometric mean, which considers that an arbitrary shaped and oriented volumes of solid is randomly distributed (Glover et al., 2000), and the modified Archie's law, in which the value of cementation exponent m implicitly relates to the electrical connectivity of the conductive phase and is thus, relevant to express bulk conductivity as melt fraction (e.g., Glover et al., 2000; Miller et al., 2015). These models correspond respectively to the following Equations 9 and 10

POMMIER ET AL. 13 of 18

$$\sigma_{bulk} = \sigma_{liq}^{X_{liq}} \times \sigma_{SiO2}^{1 - X_{liq}} \tag{9}$$

$$\sigma_{bulk} = \sigma_{SiO2} \left(1 - X_{liq} \right)^p + \sigma_{liq} X_{liq}^m \tag{10}$$

with

$$p = \frac{\log\left(1 - X_{liq}^m\right)}{\log(1 - X_{liq})} \tag{11}$$

In these equations, X_{liq} is the volume fraction of liquid, σ_i is the conductivity of phase i, and m is the cementation exponent. The melt phase being well connected, we considered a value of m=1 (± 0.3) (full connectivity is achieved for m=1; Glover et al., 2000). We observe that for both models, the metallic melt phase, which is several orders of magnitudes more conductive (or less resistive) than solid SiO₂, controls the bulk electrical response at the conditions relevant to planetary cores (i.e., for relatively small amounts of SiO₂). The addition of a small amount of SiO₂ will not change noticeably bulk conductivity, and the material properties of the two-phase system will be similar to those of the liquid until the rheological transition at around 60% solid fraction when they will exhibit more solid-like behavior. As a consequence, we assume that for small amounts of SiO₂, the measured bulk resistivity of partially molten samples containing Si is similar to that of the fully molten state.

Previous phase equilibria experiments in the Fe-S-O system under pressure and temperature conditions relevant to the cores of small terrestrial bodies have reported the presence of FeO grains coexisting with Fe grains as well as the liquid phase, and possibly forming a layer at the solid iron-liquid interface (Pommier et al., 2018; Tsuno & Ohtani, 2009; Urakawa et al., 1987). Our quenched Fe-S-O(-Si) samples do not show the presence of solid FeO coexisting with the liquid phase, which can be explained by the high quenching temperatures of the experiments (the Mg-bearing samples were quenched at too low T to have a significant proportion of melt). Liquid immiscibility in Fe-S-O alloys has also been reported at T > 2100 K and over the 15–21 GPa pressure range, with the immiscibility gap disappearing at pressure higher than 21 GPa (e.g., Tsuno et al., 2007). Immiscibility depends on the pressure and temperature conditions as well as the respective amounts of alloying agents, as previously observed for the Fe-S-O samples that were quenched at a temperature significantly lower than 2100 K, and thus, it is not a parameter in the models. We identified it in the Mg,Si-bearing material (Figure 2), but further work is required to constrain the phase diagram for this composition.

4.2. The Effect of Multiple Alloys on the Cooling and Dynamo of Small Terrestrial Bodies

Applied to Mars, our results suggest that the thermal conductivity values (Figure 5) are significantly lower than the values of 40-50 W m⁻¹ K⁻¹ used in previous studies of Martian core thermal-magnetic evolution (Davies & Pommier, 2018; O'Rourke & Shim, 2019; Williams & Nimmo, 2004). This observation can be explained by the fact that these studies either varied thermal conductivity in order to get the dynamo to fail at a specific time, rather than drawing on experimental results (O'Rourke & Shim, 2019), or used thermal conductivity estimates from previous studies on Fe and binary alloys (Davies & Pommier, 2018; Williams & Nimmo, 2004). We have shown that it is possible to reconcile the inferred termination time of the dynamo with the low k values by varying the CMB heat flow, Q_{cmb} , based on a simple empirical relation. In reality, the CMB heat flow is set by mantle convection and future work modeling 3-D mantle convection is required to establish whether the obtained time series of CMB are dynamically consistent. We find that our Q_{cmb} time series for the FeS₅O_{0.5} composition is consistent with the results from Williams and Nimmo (2004) and Leone et al. (2014), while the time series for the FeS₅O_{0.3}Si₁ composition exhibits similar long-term behavior compared to the Leone et al. (2014) result but with a sharper initial decline that is similar to the calculation of Thiriet et al. (2019). The magnitude of the initial decline in heat flow depends on the degree to which the core is superheated compared to the mantle, which is poorly constrained. We therefore suggest that the heat flows we have obtained are plausible and that the reported Martian thermal-magnetic evolutionary scenarios for each of the three chosen compositions are compatible with the inferred termination time of the dynamo. Regarding core chemistry, the fact that none of the models from Figure 7 produced a snow zone

POMMIER ET AL. 14 of 18



suggests that low oxygen concentrations are required for the Martian core to preserve a snow zone at the present day.

For the Moon, it has been suggested that a magnetic field existed between at least 4.2 and 3.56 Ga (Laneuville et al., 2014). Assuming an Fe-FeS composition and a k value of 50 W m⁻¹ K⁻¹ (using de Koker et al., 2012), Laneuville and coworkers proposed a possible core cooling scenario to reproduce the paleomagnetic constraints that consists of the growth of an inner core by a transition between a bottom-up and top-down core crystallization (Laneuville et al., 2014). Our results suggest that much lower k values than 50 W m⁻¹ K⁻¹ are to be expected for an O-bearing lunar core, even if the effect of pressure on k should increase thermal conductivity by a factor of ~2 at the pressure conditions of the Moon, considering the effect of pressure on k from previous studies (e.g., Pommier, 2018; Secco, 2017). These low k values could question the need for a transition in the core crystallization regime. The Galilean satellite Ganymede presents an intrinsic magnetic field that is consistent with a snow regime in its core, assuming a pure Fe composition (Rückriemen et al., 2015). In this modeling study, k was varied from 20 to 60 W m⁻¹ K⁻¹. Based on our results, we can speculate that in the case of an O-bearing core, much lower thermal conductivities could maintain the dynamo active through time.

5. Conclusions

This multidisciplinary investigation of iron alloys containing multiple alloying agents (S, O, Si, Mg) shows that at $T>1200~\rm K$ and $P=10~\rm GPa$, electrical resistivity of O-bearing iron alloys increases slightly with increasing T and significantly with the total amount of alloying agents, indicating that the effect of chemistry on the electrical properties is important and should be accounted for as part of core cooling models. The electrical measurements and thermal conductivity estimates of these alloys reveal a complex interplay and a different structural behavior of S, O, Si, and possibly, Mg. Applied to the metallic core of a small terrestrial body, our results suggest that bulk chemistry significantly affects the power available to drive the dynamo during core cooling. In particular, an application to the Martian core using the CMB heat flow from Williams and Nimmo (2004) indicates that the presence of oxygen would delay considerably the dynamo cessation as well as the formation of a snow zone, compared to an O-free, Fe-S core. It is possible to match the dynamo termination time for each k value by changing the CMB heat flow, with high oxygen concentrations requiring a high initial heat flow and more rapid decline in order to match the inferred timing of Martian dynamo failure. Our results demonstrate that thermal conductivities can change the dynamo cessation time significantly, by a billion years or more.

Data Availability Statement

Data sets for this research are deposited in the Dryad repository (https://doi.org/10.6075/J0W37TTW).

References

- Acuña, M. H., Connerney, J. E. P., Wasilewski, P., Lin, R. P., Anderson, K. A., Carlson, C. W., et al. (1998). Magnetic field and plasma observations at Mars: Initial results of the Mars global surveyor mission. *Science*, 279(5357), 1676–1680. https://doi.org/10.1126/science.279.5357.1676
- Alfè, D., & Gillan, M. J. (1998). First-principles simulations of liquid Fe-S under Earth's core conditions. *Physical Review B*, 58(13), 8248. https://doi.org/10.1103/PhysRevB.58.8248
- Alfè, D., Price, G. D., & Gillan, M. J. (2002). Iron under Earth's core conditions: Liquid-state thermodynamics and high-pressure melting curve from *ab initio* calculations. *Physical Review B*, 65(16). https://doi.org/10.1103/physrevb.65.165118
- Badro, J., Brodholt, J. P., Piet, H., Siebert, J., & Ryerson, F. J. (2015). Core formation and core composition from coupled geochemical and geophysical constraints. *Proceedings of the National Academy of Sciences*, 112(40), 12310–12314. https://doi.org/10.1073/pnas.1505672112
- Badro, J., Fiquet, G., Guyot, F., Gregoryanz, E., Occelli, F., Antonangeli, D., & d'Astuto, M. (2007). Effect of light elements on the sound velocities in solid iron: Implications for the composition of Earth's core. Earth and Planetary Science Letters, 254(1–2), 233–238. https://doi.org/10.1016/j.epsl.2006.11.025
- Badro, J., Siebert, J., & Nimmo, F. (2016). An early geodynamo driven by exsolution of mantle components from Earth's core. *Nature*, 536(7616), 326–328. https://doi.org/10.1038/nature18594
- Breuer, D., & Moore, B. (2015). Dynamics and thermal history of the terrestrial planets, the Moon, and Io. In G. Schubert (Ed.), *Treatise on Geophysics* (Vol. 10, pp. 255–305). Berlin-Adlershof: Elsevier. https://doi.org/10.1016/B978-0-444-53802-4.00166-4
- Breuer, D., Rueckriemen, T., & Spohn, T. (2015). Iron snow, crystal floats, and inner-core growth: Modes of core solidification and implications for dynamos in terrestrial planets and moons. *Progress in Earth and Planetary Science*, 2(1), 1–26. https://doi.org/10.1186/s40645-015-0069-y

Acknowledgments

This project was supported by NSF-NERC Grant 1832462 awarded to A. P. and C. J. D. A. P. gratefully acknowledges support from NSF-CAREER Award 1750746. C. J. D. also gratefully acknowledges support from a Natural Environment Research Council Independent Research Fellowship (NE/L011328/1). A. P. acknowledges financial support from an NSF-COMPRES IV EOID subaward. Use of the COMPRES Cell Assembly Project was also supported by COMPRES under NSF Cooperative Agreement EAR 1661511, and A. P. thanks Kurt Leinenweber (ASU) for providing the cell assemblies. We thank the SEM Facility at UCSD and in particular, Sabine Faulhaber for her assistance with SEM analyses. We thank two anonymous reviewers for their comments that improved the manuscript and Laurent Montesi for his editorial work.

POMMIER ET AL. 15 of 18



- Buono, A. S., & Walker, D. (2011). The Fe-rich liquidus in the Fe-FeS system from 1 bar to 10 GPa. Geochimica et Cosmochimica Acta, 75(8), 2072–2087. https://doi.org/10.1016/j.gca.2011.01.030
- Buono, A. S., & Walker, D. (2015). H, not O or pressure, causes eutectic T depression in the Fe-FeS system to 8 GPa. *Meteoritics & Planetary Science*, 50(4), 547–554. https://doi.org/10.1111/maps.12372
- Cartier, C., Namur, O., Nittler, L. R., Weider, S. Z., Crapster-Pregont, E., Vorburgerf, A., et al. (2020). No FeS layer in Mercury? Evidence from Ti/Al measured by MESSENGER. *Earth and Planetary Science Letters*, 534, 116,108.
- Chen, B., Gao, L., Leinenweber, K., Wang, Y., Sanehira, T., & Li, J. (2008). In situ investigation of high-pressure melting behavior in the Fe-S system using synchrotron X-ray radiography. *High Pressure Research*, 28(3), 315–326. https://doi.org/10.1080/08957950802318883
- Davies, C. J. (2015). Cooling history of Earth's core with high thermal conductivity. *Physics of the Earth and Planetary Interiors*, 247, 65–79. https://doi.org/10.1016/j.pepi.2015.03.007
- Davies, C. J., & Pommier, A. (2018). Iron snow in the Martian core? Earth and Planetary Science Letters, 481, 189–200. https://doi.org/ 10.1016/j.epsl.2017.10.026
- Davies, C. J., Pozzo, M., Gubbins, D., & Alfè, D. (2015). Constraints from material properties on the dynamics and evolution of Earth's core. Nature Geoscience, 8(9), 678–685. https://doi.org/10.1038/ngeo2492
- de Koker, N., Steinle-Neumann, G., & Vlček, V. (2012). Electrical resistivity and thermal conductivity of liquid Fe alloys at high *P* and *T*, and heat flux in Earth's core. *Proceedings of the National Academy of Sciences*, *109*(11), 4070–4073. https://doi.org/10.1073/pnas.1111841109
- Deng, L., Seagle, C., Fei, Y., & Shahar, A. (2013). High pressure and temperature electrical resistivity of iron and implications for planetary cores. *Geophysical Research Letters*, 40, 33–37. https://doi.org/10.1029/2012GL054347
- Dobson, D. (2016). Earth's core problem. Nature, 534(7605), 45-45. https://doi.org/10.1038/534045a
- Dreibus, G., & Wanke, H. (1985). Mars, a volatile-rich planet. Meteoritics, 20, 367-381.
- Franz, R., & Wiedemann, G. (1853). Ueber die Wärme-Leitungsfähigkeit der Metalle. Annalen der Physik, 165(8), 497–531. https://doi.org/10.1002/andp.18531650802
- Glover, P. W., Hole, M. J., & Pous, J. (2000). A modified Archie's law for two conducting phases. Earth and Planetary Science Letters, 180(3–4), 369–383.
- Gomi, H., & Hirose, K. (2015). Electrical resistivity and thermal conductivity of hcp Fe–Ni alloys under high pressure: Implications for thermal convection in the Earth's core. *Physics of the Earth and Planetary Interiors*, 247, 2–10. https://doi.org/10.1016/j.pepi.2015.04.003
- Gomi, H., Hirose, K., Akai, H., & Fei, Y. (2016). Electrical resistivity of substitutionally disordered hcp Fe–Si and Fe–Ni alloys: Chemically-induced resistivity saturation in the Earth's core. *Earth and Planetary Science Letters*, 451, 51–61. https://doi.org/10.1016/j.epsl.2016.07.011
- Gomi, H., Ohta, K., Hirose, K., Labrosse, S., Caracas, R., Verstraete, M. J., & Hernlund, J. W. (2013). The high conductivity of iron and thermal evolution of the Earth's core. *Physics of the Earth and Planetary Interiors*, 224, 88–103. https://doi.org/10.1016/j.pepi.2013.07.010
- Gubbins, D., Alfè, D., Davies, C., & Pozzo, M. (2015). On core convection and the geodynamo: Effects of high electrical and thermal conductivity. *Physics of the Earth and Planetary Interiors*, 247, 56–64. https://doi.org/10.1016/j.pepi.2015.04.002
- Hauck, S. A., Aurnou, J. M., & Dombard, A. J. (2006). Sulfur's impact on core evolution and magnetic field generation on Ganymede. Journal of Geophysical Research, 111, E09008. https://doi.org/10.1029/2005JE002557
- Hauck, S. A., Margot, J. L., Solomon, S. C., Phillips, R. J., Johnson, C. L., Lemoine, F. G., et al. (2013). The curious case of Mercury's internal structure. *Journal of Geophysical Research: Planets*, 118(6), 1204–1220. https://doi.org/10.1002/jgre.20091
- Hirose, K., Labrosse, S., & Hernlund, J. (2013). Composition and state of the core. Annual Review of Earth and Planetary Sciences, 41, 657–691
- Ho, C.Y., Ackerman, M.W., Wu, K.Y., Oh, S.G., Havill, T.N. (1975). Thermal conductivity of ten selected binary alloy systems. CINDAS-TPRC Report 30, Office of Standard Reference Data, National Bureau of Standards, U.S. Department of Commerce, Washington, DC.
- Holder, T. K. (1977). Thermal conductivity, electrical resistivity and Seebeck coefficient of high purity iron and selected iron alloys from 90 K to 400 K. Oak Ridge, TN: Oak Ridge National Laboratory. https://doi.org/10.2172/7107964
- Huang, H., Hu, X., Jing, F., Cai, L., Shen, Q., Gong, Z., & Liu, H. (2010). Melting behavior of Fe-O-S at high pressure: A discussion on the melting depression induced by O and S. *Journal of Geophysical Research*, 115, B05207. https://doi.org/10.1029/2009JB006514
- Kimura, T., Ohfuji, H., Nishi, M., & Irifune, T. (2017). Melting temperatures of MgO under high pressure by micro-texture analysis. *Nature Communications*, 8(1), 1–7. https://doi.org/10.1038/ncomms15735
- Kita, Y., & Morita, Z. I. (1984). The electrical resistivity of liquid Fe-Ni, Fe-co and Ni-co alloys. *Journal of Non-Crystalline Solids*, 61, 1079–1084. https://doi.org/10.1016/0022-3093(84)90684-7
- Knibbe, J. S., & van Westrenen, W. (2018). The thermal evolution of Mercury's Fe-Si core. Earth and Planetary Science Letters, 482, 147–159
- Konôpková, Z., McWilliams, R. S., Gómez-Pérez, N., & Goncharov, A. F. (2016). Direct measurement of thermal conductivity in solid iron at planetary core conditions. *Nature*, 534(7605), 99–101. https://doi.org/10.1038/nature18009
- Kuskov, O., & Belashchenko, D. (2016). Molecular dynamics estimates for the thermodynamic properties of the Fe-S liquid cores of the Moon, Io, Europa, and Ganymede. Solar System Research, 50(3), 165–183. https://doi.org/10.1134/S0038094616030035
- Labrosse, S. (2015). Thermal evolution of the core with a high thermal conductivity. *Physics of the Earth and Planetary Interiors*, 247, 36–55. Laneuville, M., Wieczorek, M., Breuer, D., Aubert, J., Morard, G., & Rückriemen, T. (2014). A long-lived lunar dynamo powered by core crystallization. *Earth and Planetary Science Letters*, 401, 251–260. https://doi.org/10.1016/j.epsl.2014.05.057
- Langlais, B., et al. (2012). A late Martian dynamo cessation time 3.77 Gy Aga. Lunar planet. Sci. Conf. 43, 1231
- Leone, G., Tackley, P. J., Gerya, T. V., May, D. A., & Zhu, G. (2014). Three-dimensional simulations of the southern polar giant impact hypothesis for the origin of the Martian dichotomy. *Geophysical Research Letters*, 41, 8736–8743. https://doi.org/10.1002/2014GL062261 Lodders, K., & Fegley, B. Jr. (1997). An oxygen isotope model for the composition of Mars. *Icarus*, 126(2), 373–394. https://doi.org/10.1006/
- Manthilake, G., Chantel, J., Monteux, J., Andrault, D., Bouhifd, M. A., Bolfan Casanova, N., et al. (2019). Thermal conductivity of FeS and its implications for Mercury's long-sustaining magnetic field. *Journal of Geophysical Research: Planets*, 124, 2359–2368. https://doi.org/ 10.1029/2019JE005979
- McDonough, W. F. (2003). Compositional model for the earth's core. In R. W. Carlson, H. D. Holland, & K. K. Turekianet (Eds.), treatise on geochemistry (Vol. 2, pp. 547–568). Amsterdam: Elsevier. https://doi.org/10.1016/B0-08-043751-6/02015-6
- Miller, K. J., Montési, L. G., & Zhu, W. L. (2015). Estimates of olivine-basaltic melt electrical conductivity using a digital rock physics approach. Earth and Planetary Science Letters, 432, 332–341.

POMMIER ET AL. 16 of 18



- Morard, G., & Katsura, T. (2010). Pressure–temperature cartography of Fe–S–Si immiscible system. *Geochimica et Cosmochimica Acta*, 74(12), 3659–3667. https://doi.org/10.1016/j.gca.2010.03.025
- Morard, G., Sanloup, C., Guillot, B., Fiquet, G., Mezouar, M., Perrillat, J. P., et al. (2008). In situ structural investigation of Fe-S-Si immiscible liquid system and evolution of Fe-S bond properties with pressure. *Journal of Geophysical Research: Solid Earth*, 113, B10205. https://doi.org/10.1029/2008JB005663
- Mori, Y., Ozawa, H., Hirose, K., Sinmyo, R., Tateno, S., Morard, G., & Ohishi, Y. (2017). Melting experiments on Fe–Fe3S system to 254 GPa. Earth and Planetary Science Letters, 464, 135–141. https://doi.org/10.1016/j.epsl.2017.02.021
- Namur, O., Charlier, B., Holtz, F., Cartier, C., & McCammon, C. (2016). Sulfur solubility in reduced mafic silicate melts: Implications for the speciation and distribution of sulfur on mercury. Earth and Planetary Science Letters, 448, 102–114. https://doi.org/10.1016/j. epsl.2016.05.024
- Nimmo, F. (2015). Energetics of the Core. In G. Schubert (Ed.), Treatise on Geophysics (Vol. 8, pp. 27-55). Amsterdam: Elsevier.
- Ohta, K., Kuwayama, Y., Hirose, K., Shimizu, K., & Ohishi, Y. (2016). Experimental determination of the electrical resistivity of iron at Earth's core conditions. *Nature*, 534(7605), 95–98. https://doi.org/10.1038/nature17957
- Ohtani, E., & Ringwood, A. E. (1984). Composition of the core, I. solubility of oxygen in molten iron at high temperatures. Earth and Planetary Science Letters, 71(1), 85–93. https://doi.org/10.1016/0012-821X(84)90054-2
- O'Rourke, J. G., & Shim, S. H. (2019). Hydrogenation of the Martian core by hydrated mantle minerals with implications for the early dynamo. *Journal of Geophysical Research: Planets*, 124, 3422–3441. https://doi.org/10.1029/2019JE005950
- O'Rourke, J. G., & Stevenson, D. J. (2016). Powering Earth's dynamo with magnesium precipitation from the core. *Nature*, 529(7586), 387–389. https://doi.org/10.1038/nature16495
- Poirier, J.-P. (1994). Light elements in the Earth's outer core: A critical review. Physics of the Earth and Planetary Interiors, 85(3-4), 319-337. https://doi.org/10.1016/0031-9201(94)90120-1
- Pommier, A. (2018). Influence of sulfur on the electrical resistivity of a crystallizing core in small terrestrial bodies. Earth and Planetary Science Letters, 496, 37–46. https://doi.org/10.1016/j.epsl.2018.05.032
- Pommier, A. (2020). Experimental investigation of the effect of nickel on the electrical resistivity of Fe-Ni and Fe-Ni-S alloys under pressures. American Mineralogist, 105, 1069–1077. https://doi.org/10.2138/am-2020-7301
- Pommier, A., Laurenz, V., Davies, C. J., & Frost, D. J. (2018). Melting phase relations in the Fe-S and Fe-SO systems at core conditions in small terrestrial bodies. *Icarus*, 306, 150–162. https://doi.org/10.1016/j.icarus.2018.01.021
- Pommier, A., Leinenweber, K., & Tran, T. (2019). Mercury's thermal evolution controlled by an insulating liquid outermost core? *Earth and Planetary Science Letters*, 517, 125–134. https://doi.org/10.1016/j.epsl.2019.04.022
- Pommier, A., & Leinenweber, K. D. (2018). Electrical cell assembly for reproducible conductivity experiments in the multi-anvil. American Mineralogist, 103(8), 1298–1305. https://doi.org/10.2138/am-2018-6448
- Pozzo, M., Davies, C., Gubbins, D., & Alfe, D. (2012). Thermal and electrical conductivity of iron at Earth's core conditions. *Nature*, 485(7398), 355–358. https://doi.org/10.1038/nature11031
- Pozzo, M., Davies, C., Gubbins, D., & Alfè, D. (2013). Transport properties for liquid silicon-oxygen-iron mixtures at Earth's core conditions. Physical Review B, 87(1), 014110. https://doi.org/10.1103/PhysRevB.87.014110
- Pozzo, M., Davies, C., Gubbins, D., & Alfe, D. (2019). FeO content of Earth's liquid Core. Physical review X, 9(4). p.041018
- Rubie, D. C., Jacobson, S. A., Morbidelli, A., O'Brien, D. P., Young, E. D., de Vries, J., et al. (2015). Accretion and differentiation of the terrestrial planets with implications for the compositions of early-formed solar system bodies and accretion of water. *Icarus*, 248, 89–108. https://doi.org/10.1016/j.icarus.2014.10.015
- Rückriemen, T., Breuer, D., & Spohn, T. (2015). The Fe snow regime in Ganymede's core: A deep-seated dynamo below a stable snow zone. Journal of Geophysical Research: Planets, 120, 1095–1118. https://doi.org/10.1002/2014JE004781
- Sanloup, C., Fiquet, G., Gregoryanz, E., Morard, G., & Mezouar, M. (2004). Effect of Si on liquid Fe compressibility: Implications for sound velocity in core materials. *Geophysical Research Letters*, 31, L07604. https://doi.org/10.1029/2004GL019526
- Secco, R. A. (2017). Thermal conductivity and Seebeck coefficient of Fe and Fe-Si alloys: Implications for variable Lorenz number. *Physics of the Earth and Planetary Interiors*, 265, 23–34. https://doi.org/10.1016/j.pepi.2017.01.005
- Seifter, A., Pottlacher, G., Jäger, H., Groboth, G., & Kaschnitz, E. (1998). Measurements of thermophysical properties of solid and liquid Fe-Ni alloys. Berichte der Bunsengesellschaft für Physikalische Chemie, 102(9), 1266–1271. https://doi.org/10.1002/bbpc.19981020934
- Silber, R. E., Secco, R. A., Yong, W., & Littleton, J. A. (2018). Electrical resistivity of liquid Fe to 12 GPa: Implications for heat flow in cores of terrestrial bodies. *Scientific Reports*, 8(1), 1, 10758–9. https://doi.org/10.1038/s41598-018-28921-w
- Silber, R. E., Secco, R. A., Yong, W., & Littleton, J. A. (2019). Heat flow in Earth's core from invariant electrical resistivity of Fe-Si on the melting boundary to 9 GPa: Do light elements matter? *Journal of Geophysical Research: Solid Earth*, 124, 5521–5543. https://doi.org/10.1029/2019JB017375
- Stauffer, D., & Aharony, A. (1992). Introduction to percolation theory (2nd ed., p. 192). London: Taylor & Francis. ISBN: 9781315274386. https://doi.org/10.1201/9781315274386
- Stewart, A. J., Schmidt, M. W., van Westrenen, W., & Liebske, C. (2007). Mars: A new core-crystallization regime. Science, 316(5829), 1323–1325. https://doi.org/10.1126/science.1140549
- Suehiro, S., Ohta, K., Hirose, K., Morard, G., & Ohishi, Y. (2017). The influence of sulfur on the electrical resistivity of hcp iron: Implications for the core conductivity of Mars and Earth. Geophysical Research Letters, 44, 8254–8259. https://doi.org/10.1002/2017GL074021
- ten Grotenhuis, S. M., Drury, M. R., Spiers, C. J., & Peach, C. J. (2005). Melt distribution in olivine rocks based on electrical conductivity measurement. *Journal of Geophysical Research*, 110, B12201. https://doi.org/10.1029/2004JB003462
- Terasaki, H., Kamada, S., Sakai, T., Ohtani, E., Hirao, N., & Ohishi, Y. (2011). Liquidus and solidus temperatures of a Fe–O–S alloy up to the pressures of the outer core: Implication for the thermal structure of the Earth's core. *Earth and Planetary Science Letters*, 304(3–4), 559–564. https://doi.org/10.1016/j.epsl.2011.02.041
- Thiriet, M., Breuer, D., Michaut, C., & Plesa, A.-C. (2019). Scaling laws of convection for cooling planets in a stagnant lid regime. *Physics of the Earth and Planetary Interiors*, 286, 138–153.
- Tsuno, K., Frost, D. J., & Rubie, D. C. (2011). The effects of nickel and Sulphur on the core–mantle partitioning of oxygen in earth and Mars. Physics of the Earth and Planetary Interiors, 185(1–2), 1–12. https://doi.org/10.1016/j.pepi.2010.11.009
- Tsuno, K., & Ohtani, E. (2009). Eutectic temperatures and melting relations in the Fe-O-S system at high pressures and temperatures. Physics and Chemistry of Minerals, 36(1), 9-17. https://doi.org/10.1007/s00269-008-0254-2
- Tsuno, K., Ohtani, E., & Terasaki, H. (2007). Immiscible two-liquid regions in the Fe–O–S system at high pressure: Implications for planetary cores. *Physics of the Earth and Planetary Interiors*, 160(1), 75–85. https://doi.org/10.1016/j.pepi.2006.09.004

POMMIER ET AL. 17 of 18



- Urakawa, S., Kato, M., & Kumazawa, M. (1987). Experimental study on the phase relations in the system Fe-Ni-O-S up to 15 GPa. High-Pressure Research in Mineral Physics: A Volume in Honor of Syun-iti Akimoto, 39, 95–111. https://doi.org/10.1029/GM039p0095
- Wagle, F., Steinle-Neumann, G., & de Koker, N. (2018). Saturation and negative temperature coefficient of electrical resistivity in liquid iron-sulfur alloys at high densities from first-principles calculations. *Physical Review B*, 97(9), 094307. https://doi.org/10.1103/PhysRevB.97.094307
- Wagle, F., Steinle-Neumann, G., & de Koker, N. (2019). Resistivity saturation in liquid iron–light-element alloys at conditions of planetary cores from first principles computations. Comptes Rendus Geoscience, 351(2–3), 154–162. https://doi.org/10.1016/j.crte.2018.05.002
- Watanabe, M., Adachi, M., Uchikoshi, M., & Fukuyama, H. (2019). Thermal conductivities of Fe-Ni melts measured by non-contact laser modulation calorimetry. *Metallurgical and Materials Transactions A*, 50(7), 3295–3300. https://doi.org/10.1007/s11661-019-05250-9
- Weiss, B. P., Vali, H., Baudenbacher, F. J., Kirschvink, J. L., Stewart, S. T., & Shuster, D. L. (2002). Records of an ancient Martian magnetic field in ALH84001. Earth and Planetary Science Letters, 201(3-4), 449-463. https://doi.org/10.1016/S0012-821X(02)00728-8
- Williams, J.-P., & Nimmo, F. (2004). Thermal evolution of the Martian core: Implications for an early dynamo. *Geology*, 32(2), 97–100. https://doi.org/10.1130/G19975.1
- Yin, Y., Zhai, K., Zhang, B., & Zhai, S. (2019). Electrical resistivity of iron phosphides at high-pressure and high-temperature conditions with implications for lunar core's thermal conductivity. *Journal of Geophysical Research: Solid Earth*, 124, 5544–5556. https://doi.org/10.1029/2018JB017157
- Yokoo, S., Hirose, K., Sinmyo, R., & Tagawa, S. (2019). Melting experiments on liquidus phase relations in the Fe-S-O ternary system under core pressures. *Geophysical Research Letters*, 46, 5137–5145. https://doi.org/10.1029/2019GL082277
- Zhang, J., Liebermann, R. C., Gasparik, T., Herzberg, C. T., & Fei, Y. (1993). Melting and subsolidus relations of SiO2 at 9–14 GPa. *Journal of Geophysical Research*, 98(B11), 19,785–19,793. https://doi.org/10.1029/93JB02218

POMMIER ET AL. 18 of 18